Proceedings of the Seventh International Conference on
Railway Technology: Research, Development and Maintenance
Edited by: J. Pombo
Civil-Comp Conferences, Volume 15, Paper 4.5
Civil-Comp Press, Edinburgh, United Kingdom, 2026
ISSN: 2753-3239, doi: 10.4203/ccc.15.4.5

High-Speed Rail Milling and Thermo-Mechanical Rail Surface Load Calculations via Automated Iterative Heat Flux and Temperature Exchange Between 2D and 3D Finite Element Models

A. Ambig[1,2], T. Klünsner[2], W. Daves[2], C. Czettl[3], W. Kubin[4] and T. Antretter[5]

[1] Chair of Mechanics, Montanuniversität Leoben, Austria
[2] Department of Simulation, Materials Center Leoben Forschung GmbH, Austria
[3] R&D Cutting Tools , Ceratizit Austria GmbH, Reutte, Austria
[4] Tool Technology, Linsinger Maschinenbau GmbH, Laakirchen, Austria
[5] Chair of Mechanics, Montanuniversität Leoben, Austria

Abstract

Rail milling is increasingly used for the reprofiling of the rail head as a maintenance strategy under high-speed milling conditions. Several open questions remain regarding how rail surface loading and the resulting temperature evolution influence the inelastic deformation and damage behaviour of rail and tool materials. In this study, industrial rail milling is modelled and analysed using Arbitrary Lagrangian–Eulerian-based finite element simulations. The modelling framework is applied to the milling of rail steel using cemented carbide inserts coated with titanium aluminium nitride. In contrast to earlier work, the present study provides a more detailed analysis of the thermo-mechanical response, with particular emphasis on chip formation and the associated heat transfer. Orthogonal planing simulations based on the Arbitrary Lagrangian–Eulerian framework, together with a coupled three-dimensional heat transfer model, were used to support the calibration of material and simulation parameters for rail milling. The present study contributes to a detailed numerical investigation of industrial rail milling and supports an improved understanding of loading, temperature development and deformation behaviour in rail maintenance operations.

Keywords: rail milling, finite elements, chip formation, high-speed milling, arbitrary Lagrangian–Eulerian simulations, orthogonal planing

1 Introduction

Rail reprofiling is widely used in railway maintenance to restore the geometry and surface condition of the rail head through controlled removal of Rolling Contact Fatigue (RCF) defects, thereby ensuring safe and reliable track performance. RCF defects, such as head checks, shelling, spalling, squats, corrugation and wheel burns are among the most common forms of rail surface damage [1]. In addition, surface irregularities increase vibration and dynamic loads during wheel–rail interaction, accelerating wear in critical components such as wheels, bearings and suspension systems. Therefore, achieving a smooth and consistent rail profile through precise machining is essential for extending rail service life and reducing lifecycle costs [2].

Rail defects may arise from several sources including material inhomogeneities, manufacturing processes, welding imperfections and operational loading. Although some defects originate during rail production or welding, many are initiated or propagated under repeated wheel–rail contact loads during service. If not detected and removed in time, these defects can develop into more severe surface or subsurface damage, ultimately compromising track integrity and operational safety. Consequently, preventive and corrective maintenance strategies are required to control defect evolution and prevent further deterioration of the rail surface.

In recent years, rail maintenance strategies have increasingly shifted from conventional grinding toward milling [1]. Introduced roughly 30 years ago by the Austrian company Linsinger Maschinenbau GmbH, rail milling is a non-abrasive rotational cutting process in which material is removed from the rail head in the form of recyclable metal chips [1]. As illustrated in Figure 1(a), the rail milling process consists of two stages: milling and polishing. In the milling stage, tungsten carbide–cobalt (WC–Co) hardmetal inserts (Figure 1(b)) remove surface defects and reshape the rail head geometry, leaving a periodic surface roughness on the rail surface. This roughness is subsequently removed in the polishing stage using a longitudinal grinding wheel mounted on the maintenance train just behind the milling unit. The micrograph in Figure 1(c) shows damage on the flank face of the insert caused by the combined thermal and mechanical loads in service. Quantitative information on the operational loads during the reprofiling process is essential, as it supports tool life assessment, rail surface quality control and the development of efficient rail maintenance strategies.

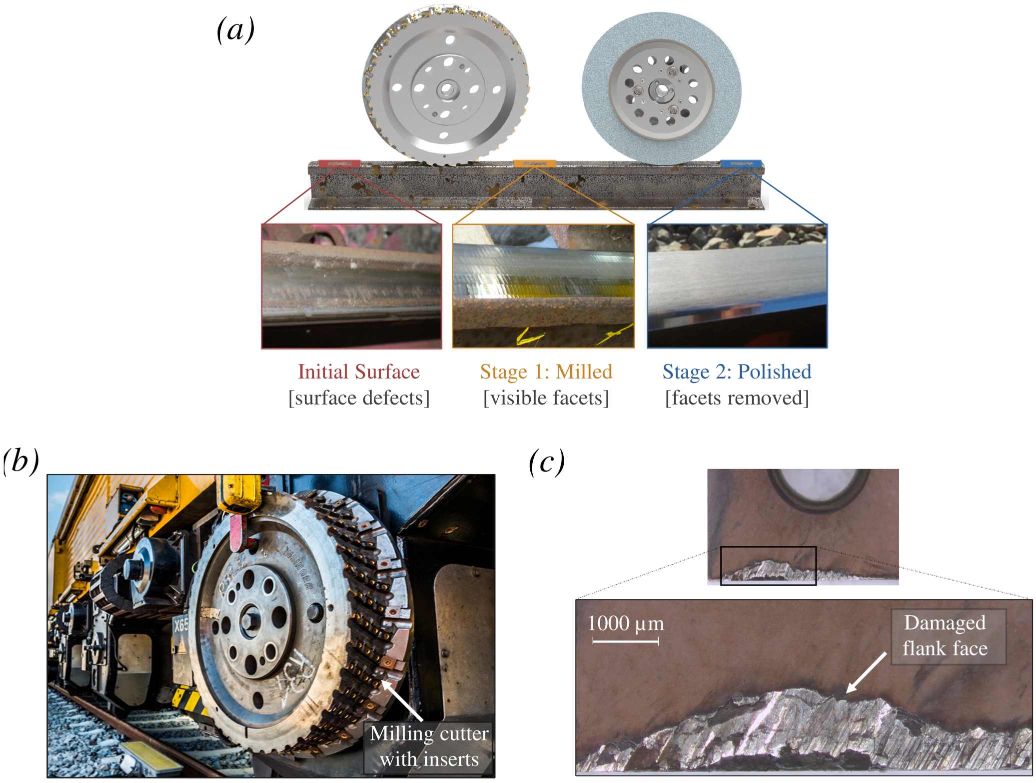

Figure 1: Rail milling process context and motivation for thermo-mechanical load analysis. (a) Two-stage rail reprofiling process. (b) Industrial rail milling unit by Linsinger Maschinenbau GmbH showing a milling cutter equipped with cutting inserts. (c) Microscopic image of a cutting insert showing a plastically deformed and worn region on the flank face, illustrating the severe loading conditions that motivate numerical simulation of forces and temperature evolution.

Numerical modelling approaches have increasingly been employed to analyse and quantify the thermal and mechanical loads generated in metal cutting operations [4–12]. Finite element (FE) modelling provides a physics-based framework for analysing chip formation and thermo-mechanical interactions during cutting processes. In particular, Arbitrary Lagrangian–Eulerian (ALE) formulations are well suited for cutting simulations because they can robustly handle large deformations and material flow while maintaining mesh quality [9, 11].

The current work focuses on the numerical investigation of industrial rail milling using two-dimensional ALE-based FE simulations. The study considers the milling of R260 rail steel using TiAlN-coated WC-Co hard metal inserts with a Co binder content of 10 wt.% and a coating thickness of 5 μm. The rail material behaviour is described by a Johnson–Cook material model [14, 15], with model parameters taken from the available literature [9, 11, 16]. In contrast to much of the earlier literature work, the applied ALE modelling framework in the current work explicitly resolves continuous chip formation during milling, thereby enabling detailed analysis of material flow and rail-tool contact evolution.

In the current study, two milling conditions with cutting speeds of 240 m/min and 380 m/min were examined. The orthogonal planing simulations together with the 2D-3D temperature mapping approach were used to support the ongoing calibration of the material and simulation parameters for rail milling. These efforts are intended to further refine the parameters for application to practical rail milling scenarios. Orthogonal planing provides a well-defined and experimentally accessible cutting configuration [17] in which force and temperature responses can be evaluated under controlled conditions while retaining the essential characteristics relevant to rail milling. To account for realistic three-dimensional heat transfer effects, a 2D-3D temperature mapping approach was implemented within the orthogonal planing simulation framework. In this approach, the 2D ALE orthogonal planing model is coupled with a 3D heat transfer model and the temperature field of the 2D ALE model is iteratively updated using a Python-based interface to improve the representation of thermo-mechanical loading at cutting tool edges.

The full calibration of the simulation parameters for rail milling is still ongoing. Nevertheless, good agreement has already been observed between orthogonal planing experiments and the corresponding simulations, indicating that the selected modelling framework and material parameters are suitable for practical rail milling applications.

2 Finite Element Analysis

2.1 2D ALE Model

In Figure 2(a), a schematic of the cutting contour generated by a single insert mounted on the tool holder is shown. The rail milling model in Figure 2(b) was prepared to simulate this contour. Additional details concerning the FE model are given in [1, 9, 16].

The analytical representation of the rail milling contour and the details of the FE model are based on the modelling framework documented in [1] and are summarised below to provide the methodological background for the current study.

In the rail milling contour shown in Figure 2(a), the feed direction is aligned with the positive x-axis, while the tool holder rotates clockwise. The black contour indicates the path left by the preceding insert and is defined by the tool holder radius R shown in the figure, where $R = D/2$ and D denotes the tool holder diameter. As the tool holder moves horizontally, the inserts consecutively engaging the rail workpiece contact the rail surface at a position offset by f_z with respect to their previous insert;

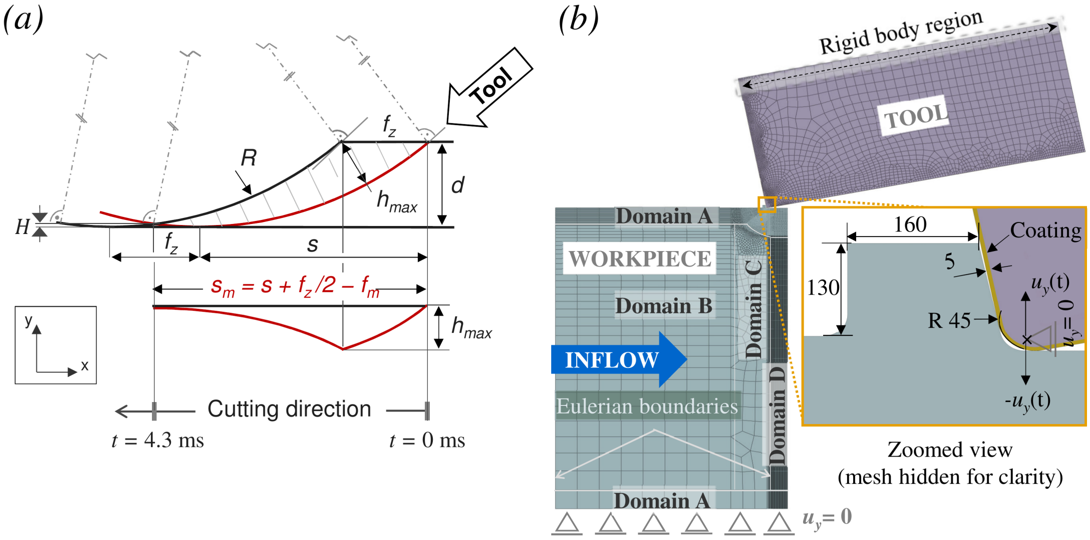

Figure 2: (a) Rail milling contour and (b) FE model used in the simulation (adapted from [1]).

this offset is termed as feed per insert. The cutting process of the insert then continues along the red contour. Consequently, the uncut chip thickness $h(t)$ varies continuously over time as each insert follows a curved path through the workpiece. The shape of the cutting trajectory depends on the chosen milling parameters (e.g. tool holder diameter, feed and cutting speed). Over the duration of one tool-workpiece engagement, the centre of the tool holder moves further in the feed direction; the associated displacement is defined as the feed per cut, f_m

In the Figure 2(a), d denotes the maximum cutting depth on the workpiece. The parameter H represents the facet height that arises from the overlap of the cutting contours of two successive inserts during the milling process. The total cutting path of one insert can be expressed analytically as shown in Eq. (1),

$$s_m = s + \frac{f_z}{2} - f_m \tag{1}$$

where s is the machining surface distance for a cut without feed rate, f_z is the feed per insert and f_m is the feed per cut. In the FE simulation of rail milling, the cutting process was modelled for a single insert mounted on the tool holder. Because of the feed motion of the tool holder center, the cutting path should be elliptical. However, since the ratio between the cutting depth d and the diameter D is small, the path was idealised as circular. The corresponding analytical calculations of the insert engagement were carried out in detail. The maximum uncut chip thickness $h_{\max}$ was evaluated along the radial direction of the tool holder. Two cutting conditions expressed as a combination of cutting speed v_c and feed per tooth f_z were considered: (1) $v_c = 240\,\mathrm{m/min}$ with $f_z = 15\,\mathrm{m/min}$ and (2) $v_c = 380\,\mathrm{m/min}$ with $f_z = 24\,\mathrm{m/min}$. In both cases, a cutting depth d of $1\,\mathrm{mm}$ and a tool holder diameter D of $600\,\mathrm{mm}$ yielded a machining surface distance of $s_m = 25.45\,\mathrm{mm}$. The corresponding maximum uncut chip thicknesses $h_{\max}$ were $389\,\mu\mathrm{m}$ and $393\,\mu\mathrm{m}$, respectively. The associated milling times t were $6.8\,\mathrm{ms}$ for $v_c = 240\,\mathrm{m/min}$ and $4.3\,\mathrm{ms}$ for $v_c = 380\,\mathrm{m/min}$. These values were obtained from a detailed analytical evaluation of the cutting contour with consideration of tool geometry and the prescribed milling parameters.

Figure 2(b) shows the FE model used in the current study for the 2D ALE rail-milling simulations previously reported in [16]. Extensive details on the modelling approach can be found in [1, 9]. The current work also applies this modelling approach to the simulation of orthogonal planing. This was also reported in [16] and is therefore not reported here again. In contrast to rail milling, the uncut chip thickness remains constant throughout the planing process. The orthogonal planing simulation was carried out for only one cutting speed namely 240 m/min, with a constant uncut chip thickness of 390 μm.

The orthogonal planing simulations will be used to calibrate key material and simulation parameters, including the heat partition ratio, the thermal conductance at the tool-workpiece interface and the Johnson–Cook parameters of the rail steel in future work. At present, both the orthogonal planing and rail milling simulations use material data and simulation parameters from the earlier work [9, 11, 16], including those for R260 rail steel, the WC-Co substrate and the TiAlN coating.

2.2 2D-3D Iterative Temperature Mapping

For the orthogonal planing simulation, a 2D-3D coupling approach was used to iteratively correct the temperature evolution predicted by the 2D ALE model. For this purpose, a 3D model based on one quarter of the insert geometry was used, as shown in Figure 3. In the orthogonal planing experiment considered here, the insert's rake face contacted the workpiece over a width of $5\,\mathrm{mm}$. The contact patch's longest dimension indicated in pink and with the upper white double-headed arrow in Figure 3, corresponds to about one third of the total insert width in the z-direction.

Figure 4 shows the automated workflow for temperature mapping. It illustrates the iterative exchange of temperature-field information between the 2D model and the 3D model in order to approximate the heat transport in the z-direction [11], as indicated in Figure 3. Neglecting this heat flow would lead to an overestimation of temperature. In the conducted orthogonal planing experiment (for details, refer [16]), the total planing time exceeded 4 s. It was therefore computationally too expensive to simulate the entire experimental planing time. Therefore, only the first 50 ms were considered in the simulation. The total simulated time, $t = 50$ ms, was divided into $k = 50$ iterations with a time increment of $\Delta t = 1$ ms, where $k = \frac{t}{\Delta t}$. The 2D model was assumed to lie in the mid-plane of the tool-workpiece contact zone at $z = 2.5$ mm in the 3D Model, see Figure 3. In each iteration, the 2D simulation was advanced by $\Delta t = 1$ ms. At the end of the two-dimensional coupled temperature-displacement simulation, the heat flux distribution along the tool-workpiece contact interface was extracted and transferred to the tool-workpiece contact interface in the 3D model, which was set up for a pure heat-transfer simulation. In order to do this, the contact

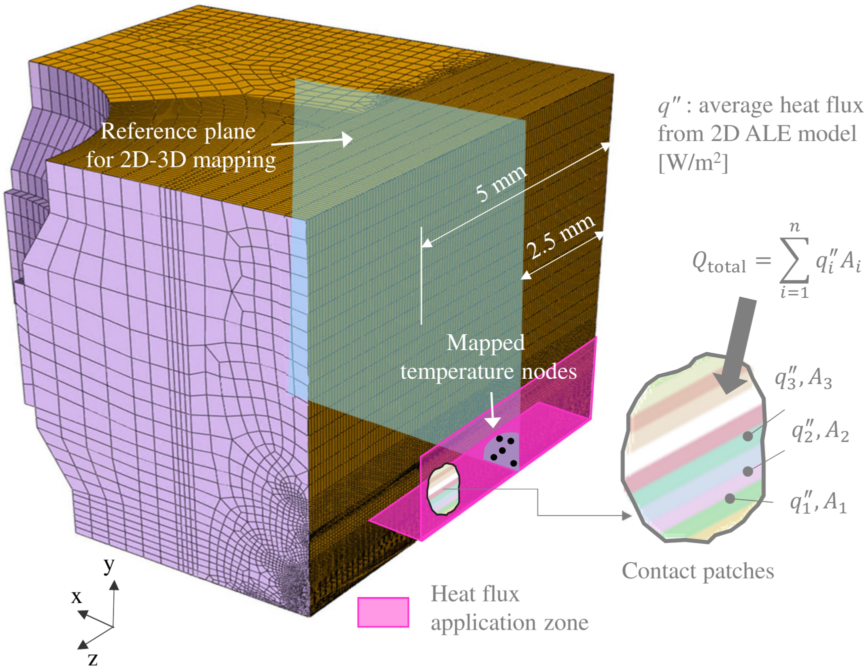

Figure 3: 3D Thermal FE model used in 2D-3D temperature mapping for the iterative calculation of the temperature during orthogonal planing simulation (see in Figure 2b).

region was discretised into consecutive edge segments (see Figure 3 and Step 3 in Figure 4), where the segment indices i were defined by neighbouring nodes a and b. The average heat flux intensity was computed as

$$q''_{m,i} = \frac{q''_{a,i} + q''_{b,i}}{2}. \tag{2}$$

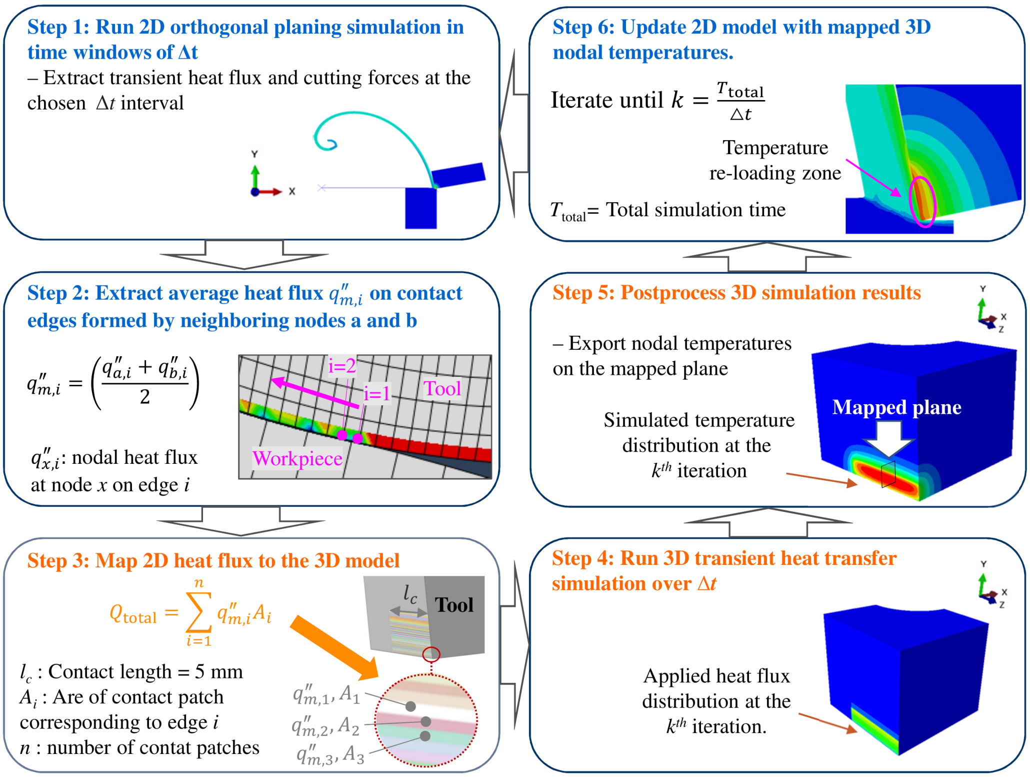

Figure 4: 2D-3D coupling procedure implemented for iteratively correcting the temperature results in 2D orthogonal planing simulation.

Here, $q''_{m,i}$ denotes the mean surface heat flux intensity (heat flow rate per unit area) transferred from the 2D contact edge segment and applied to the corresponding mapped 3D contact patch. The subscript m indicates the mean value, while the double prime indicates that the quantity is expressed per unit area. Each 2D edge segment is mapped to a corresponding 3D contact patch by extruding it over the contact engagement width $w = 5$ mm along the z-direction. The resulting contact patch area is therefore $A_i = l_i\, w$, where l_i is the edge length of the 2D contact line segment formed by nodes a and b. The resulting piecewise constant heat flux field is applied to the 3D model as a distributed surface heat flux (Neumann) boundary condition. The total heat input associated with the mapped contact region may be written in continuous form as

$$Q(\tau) = \int_{A_c} q''(\tau)\,\mathrm{d}A, \qquad 0 \leq \tau \leq \Delta t, \tag{3}$$

where A_c denotes the total contact surface area formed by the union of the n contact patches with areas A_i, $\mathrm{d}A$ is an infinitesimal surface element on A_c, and τ denotes the time within the current 2D-3D coupling time increment duration Δt. Using the discretisation of the total tool-workpiece contact area into n contact patches, the total heat input in the 3D model from the 2D model is approximated as

$$Q(\tau) \approx \sum_{i=1}^{n} q''_{m,i}(\tau)\, A_i. \tag{4}$$

In the 3D model, convection and radiation were prescribed on all non-contact free surfaces of the insert using $h = 75\,\mathrm{kW\,m^{-2}\,K^{-1}}$, $\varepsilon = 0.75$ and an ambient temperature of $20\,°\mathrm{C}$. The transient 3D heat-transfer analysis was performed over the same time increment Δt as in the corresponding 2D ALE simulation. After each 3D step, the temperature field on the mapped plane near the contact region was extracted and imposed on the corresponding nodes of the 2D model as Dirichlet temperature boundary conditions (see Figure 3 and Steps 5 and 6 in Figure 4). This iterative exchange of heat flux and temperature between the 2D and 3D models was repeated until the total simulation time t was reached.

3 Results and Discussion

3.1 Orthogonal Planing Simulation

The temperature distribution in the 2D and 3D models at the end of the simulation is shown in the contour plot in Figure 5(a) and Figure 5(b) respectively. The 3D plot indicates improved heat transfer in the z dimension. Careful observation also shows that the temperature predicted by the 2D simulation is plausible at the mapped plane in the 3D model, which is located 2.5 mm from the right edge of the 3D model shown in Figure 5b) (see also Figure 3).

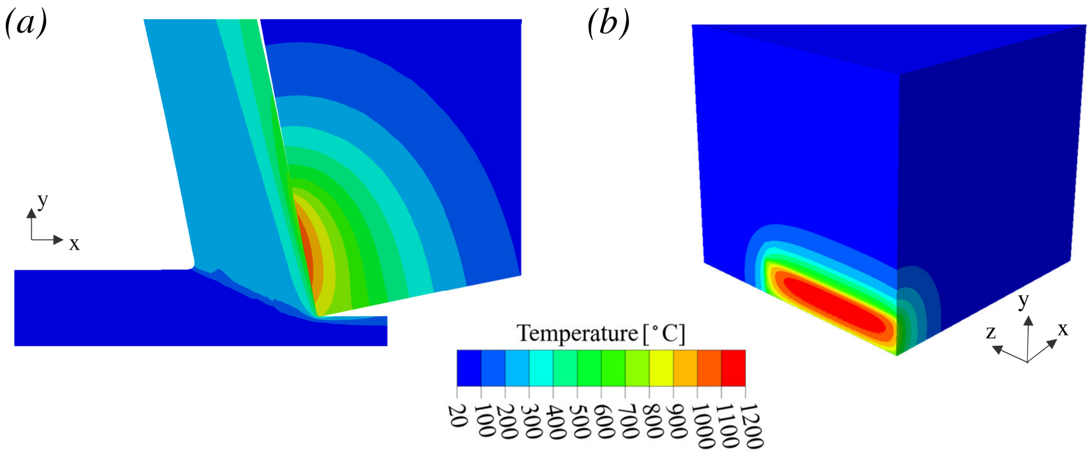

Figure 5: Temperature distribution after 50 ms in the orthogonal planing simulation for (a) the 2D model and (b) the 3D model.

The temperature results shown in Figure 5 are lower than those published in earlier work reported in [16], which was based on a 2D model. The current 2D-3D iterative mapping appears to provide a realistic representation of 3D heat transfer. However, a detailed assessment of the model is still required before any firm conclusions can be drawn. At present, the experimental force and temperature data are being compared with the simulation results and the material and simulation parameters are being calibrated to accurately represent the experimental observations. The measurement point locations of the temperature sensors and the details of the force measurements are already provided in [1]. The material and simulation parameters used in the orthogonal planing simulations were subsequently implemented in the rail milling simulation.

3.2 Rail Milling Simulations

In milling, the actual machining distance s_m during a single insert engagement is governed by the engagement geometry and process kinematics and therefore depends on parameters such as cutter diameter D, depth of cut d, feed per tooth f_z and cutting speed v_c. To compare the two cutting speeds, the machining distance was approximated as $s_m = v_c t$. Based on this approximation, the plotted states were selected to represent approximately the same machining distance s_m.

Accordingly, Figure 6 shows the deformed configurations from the 2D ALE rail milling simulations at selected times for cutting speeds of $v_c = 240$ m/min and $v_c = 380$ m/min. The plots show that cutting speed strongly influences chip flow and tool-chip interaction. At $v_c = 380$ m/min, the chip flow orientation differs clearly from that at $v_c = 240$ m/min. It can be seen from the plots that the chip becomes longer and less curled as the cutting speed increases.

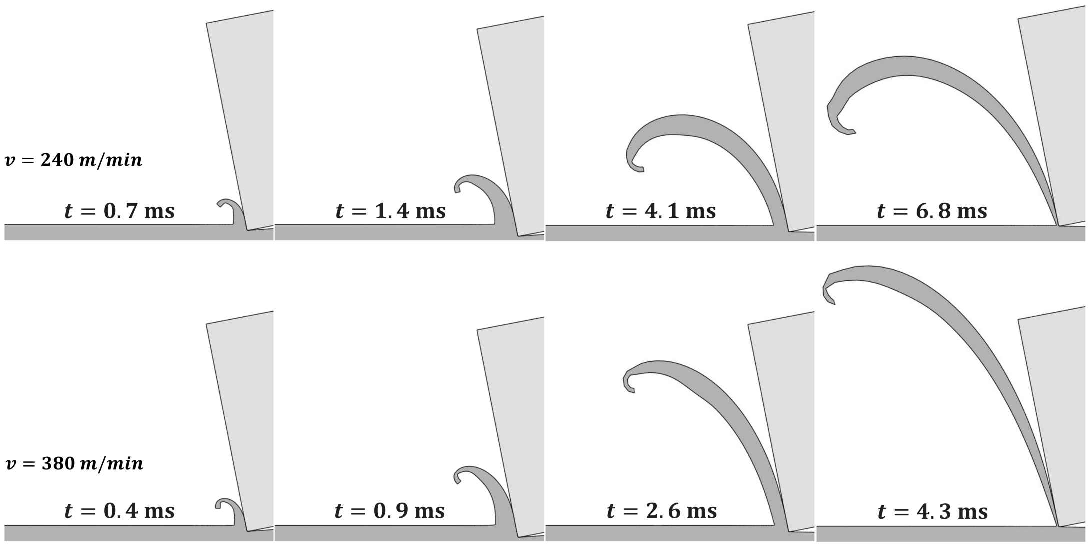

Figure 6: Chip shape evolution in 2D rail milling simulations at cutting speeds of $v_c = 240$ m/min ($h_{\max} = 389$ μm) and $v_c = 380$ m/min ($h_{\max} = 393$ μm). Workpiece: R260.

The deformation plots at different stages shown in Figure 6 reflect the orientation of chip flow, capture how the chip material moves along the tool-workpiece contact interface and how the contact area evolves with changes in chip geometry during milling. Reduced chip curling corresponds to increased tool-chip contact area and a more gradual flow of the chip along the tool surface, while more pronounced chip curling indicates reduced contact area and a sharper change in chip flow orientation. These observations suggest a more extended contact of the chip along the tool rake face at the higher cutting speed. As a result, the effective tool–chip contact length and the contact surface area are expected to be higher at the higher cutting speed. This is important because a larger contact area can lead to higher frictional heat generation and higher thermal loading, which has direct implications for milling tool design.

Figure 7 shows temperature contour plots for cutting speeds of 240 m/min and 380 m/min at different milling times t corresponding to the same machining distances s_m. The plots illustrate how the temperature distribution evolves with increasing milling time and changing depth of cut. For both cutting conditions, the temperature rises progressively in the chip and in the tool as the milling progresses. A clear difference can be observed between the two cutting speeds in terms of the temperature level within the process zone during milling.

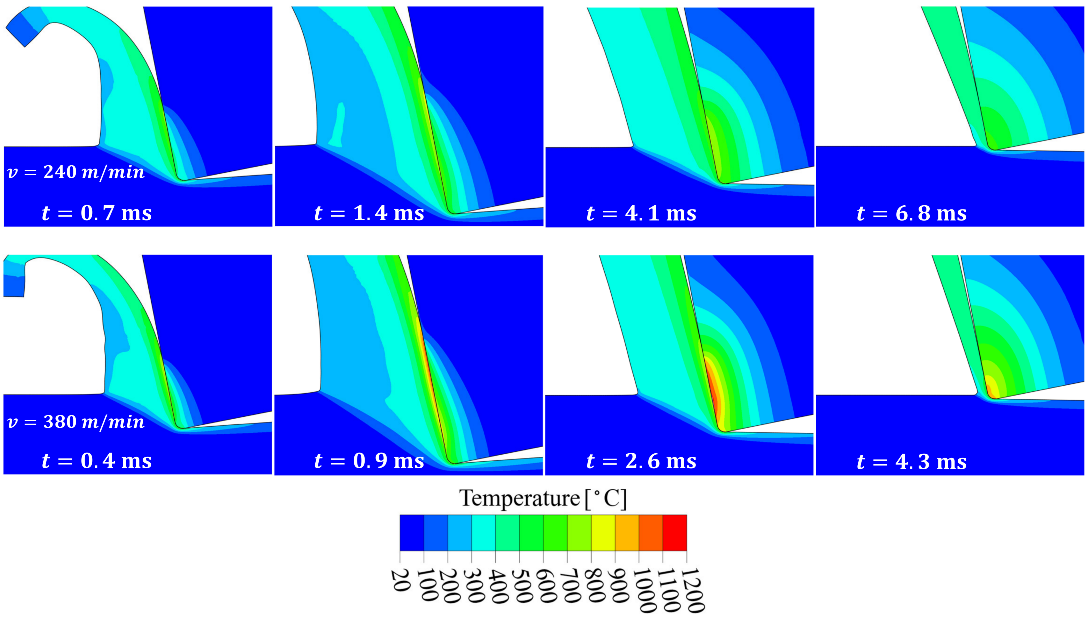

Figure 7: Temperature contours in the tool, chip, and workpiece regions during 2D ALE rail milling at cutting speeds of 240 m/min ($h = 389\,\mu$m) and 380 m/min ($h = 393\,\mu$m). Workpiece: R260.

At the higher cutting speed of 380 $\mathrm{m/min}$ the maximum tool temperature reached nearly $1200\,^{\circ}\mathrm{C}$ at $t = 2.6$ ms. At the corresponding machining distance s_m for 240 $\mathrm{m/min}$, that is at $t = 4.1$ ms, the maximum tool temperature was only in the range of $800\,^{\circ}\mathrm{C}$ to $900\,^{\circ}\mathrm{C}$. By the end of the simulation, the tool tip temperature at 380 $\mathrm{m/min}$ remained in the range of $900\,^{\circ}\mathrm{C}$ to $1000\,^{\circ}\mathrm{C}$, whereas at 240 $\mathrm{m/min}$ it was only about $600\,^{\circ}\mathrm{C}$ to $700\,^{\circ}\mathrm{C}$.

From the contour plots no clear distinction can be made between the chip temperatures observed at the two cutting speeds except at $t = 0.9$ ms for the case with 380 $\mathrm{m/min}$. At this stage the chip temperature was between $1000\,^{\circ}\mathrm{C}$ and $1100\,^{\circ}\mathrm{C}$. At the same machining distance for $240\ \mathrm{m/min}$ corresponding to $t = 1.4\ \mathrm{ms}$ the chip temperature was between $800\,^{\circ}\mathrm{C}$ and $900\,^{\circ}\mathrm{C}$. By the end of the simulation the chip temperature was nearly the same for both cutting speeds.

The temperature on the machined rail surface did not exhibit any significant increase during or after the cut. The contour plots indicate only negligible thermal penetration below the machined rail surface. These findings suggest that most of the generated heat is transferred into the chip and the tool.

Figure 8(a) shows the locations of nodes of the FE model used for analysis of their transient temperature evolution. Figure 8(b) shows the temperature evolution at these nodes during milling as a function of machining distance. Solid lines represent 380 m/min and dashed lines represent 240 m/min.

The tool tip temperature T_A exhibits rapid fluctuations, which may be attributed to factors such as changing contact conditions at the tool-workpiece interface and inertia effects. It reaches a peak value of approximately 1100°C for 380 m/min and 750°C for 240 m/min. The temperature at the substrate-coating interface T_B reaches a maximum value of approximately 950°C for 380 m/min, while under 240 m/min it reaches a maximum of about 650°C when the mean temperature trend is considered. The machined rail surface temperature at T_C remains well below the pearlitic transformation range for both cutting speeds, which is approximately 723°C for R260. At $380\ \mathrm{m/min}$ a maximum temperature of about 400°C is observed at the beginning of the process, after which the temperature decreases rapidly to around 150°C by the end of the simulation. This indicates that thermally induced bulk phase transformation is unlikely and that the bulk microstructural integrity of the rail can be expected to be preserved. However, localised microstructural modification at the immediate surface may still occur as reported in [1].

4 Concluding remarks

1. An ALE-based finite element framework was extended for the numerical simulation of orthogonal planing and used to calibrate material data for industrial rail milling.

2. The orthogonal planing simulations applied an automated iterative exchange of temperature fields and heat fluxes between consecutively executed fully coupled 2D and purely thermal 3D FE models. Compared with the pure plane-strain modelling approach, the predicted temperature levels were lower, which indicates that the present method more realistically captures three-dimensional heat transfer during planing.

3. In the rail milling simulations at 240 m/min and 380 m/min, the machined rail surface temperature remained below the pearlitic transformation range in both cases, while the maximum tool tip temperature reached approximately 750°C at 240 m/min and 1100°C at 380 m/min.

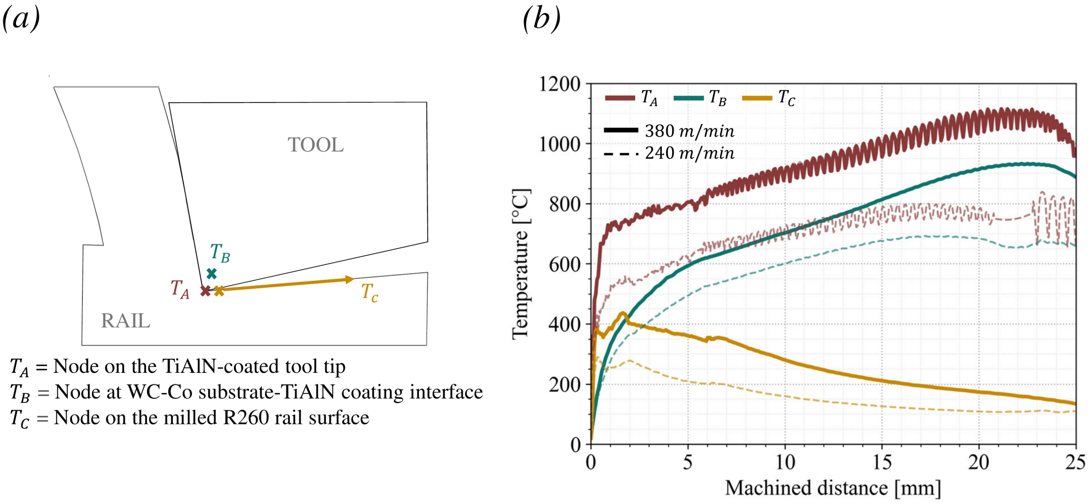

Figure 8: (a) Locations of the temperature evaluation points. (b) Temperature evolution in the tool, chip and workpiece during 2D ALE rail milling at cutting speeds of 240 m/min ($h_{\max} = 389\,\mu\text{m}$) and 380 m/min ($h_{\max} = 393\,\mu\text{m}$) for workpiece material R260. Solid lines indicate 380 m/min and dashed lines indicate 240 m/min.

4. Future work will focus on calibrating the material and simulation parameters for rail milling and on developing a full-scale rail milling model that incorporates three-dimensional heat transfer. In addition, the calculated temperatures will be validated through experimental measurement of tool temperature on multiple locations in the tool and metallographic investigations of the chip, tool and workpiece.

Acknowledgements

The authors acknowledge financial support from the COMET program through the K2 Center IC-MPPE (Project No. 886385), funded by the Austrian Ministries BMWET and BMIMI, the Austrian Research Promotion Agency (FFG) and the federal states of Styria, Upper Austria and Tyrol.

References

[1] W. Kubin, Improvement of the rail milling process & Evaluation of its potential for the reduction of rail defects, PhD thesis, Technical University of Leoben, Leoben, Austria, 2019.

[2] W. Daves, W. Kubin, S. Scheriau, M. Pletz, A finite element model to simulate the physical mechanisms of wear and crack initiation in wheel/rail contact, Tribology International, Vol. 366–367, pp. 78–83, 2016.

[3] W. Kubin, Rad-Schiene-Kontaktoptimierung mittels Schienenfräsen: Über die kontaktmechanische und werkstoffliche Optimierung der Schienen im Gleis nach der Fräsbearbeitung zur Verlängerung der Liegedauer, Der Eisenbahningenieur, Issue 09, 2021.

[4] I. Krajinović, W. Daves, M. Tkadlecz, T. Teppernegg, T. Klünsner, N. Schalk, C. Mitterer, C. Tritremmel, W. Ecker, C. Czettl, Finite element study of the influence of hard coatings on hard metal tool loading during milling, Surface & Coatings Technology, Vol. 304, pp. 134–141, 2016.

[5] L. Olovsson, L. Nilsson, K. Simonsson, An ALE formulation for the solution of two-dimensional metal cutting problems, Computers & Structures, Vol. 72, pp. 497–507, 1999.

[6] M. Movahhedy, M. S. Gadala, Y. Altintas, Simulation of the orthogonal metal cutting process using an arbitrary Lagrangian-Eulerian finite-element method, Journal of Materials Processing Technology, Vol. 103, pp. 267–275, 2000.

[7] M. H. Miguélez, A. Munoz-Sanchez, J. L. Cantero, J. A. Loya, An efficient implementation of boundary conditions in an ALE model for orthogonal cutting, Journal of Theoretical and Applied Mechanics, Vol. 47, pp. 599–616, 2009.

[8] T. Schermann, J. Marsolek, C. Schmidt, J. Fleischer, Aspects of the simulation of a cutting process and the dynamic behavior of the machine tool, CIRP International Workshop on Modelling of Machining Operations, Vol. 9, pp. 163–170, 2006.

[9] W. Kubin, W. Daves, R. Stock, Analysis of rail milling as a rail maintenance process: Simulations and experiments, Wear, Vol. 438–439, Article 203029, 2019.

[10] T. Kaltenbrunner, K. Maier, T. Klünsner, H. P. Krückl, M. Krobath, M. Pötz, J. Wosik, O. Binder, T. Teppernegg, C. Czettl, W. Ecker, Combined experimental and numerical analysis of critical loading conditions for hard metal tool damage in titanium milling, Journal of Manufacturing Processes, Vol. 90, 2023.

[11] A. W. Nemetz, W. Daves, T. Klünsner, C. Praetzas, W. Liu, T. Teppernegg, C. Czettl, F. Haas, C. Bölling, J. Schäfer, Experimentally validated calculation of the cutting edge temperature during dry milling of Ti6Al4V, Journal of Materials Processing Technology, Vol. 278, Article 116544, 2020.

[12] Y. Avevor, J. Vincent, L. Faure, A. Moufki, S. Philippon, An ALE approach for the chip formation process in high speed machining with transient cutting conditions: modeling and experimental validation, International Journal of Mechanical Sciences, Vol. 130, pp. 546–557, 2017.

[13] P. Liu, Y. Quan, J. Wan, Finite element simulations of rail milling based on the modified Johnson–Cook constitutive model, Journal of Physics: Conference Series, Vol. 1759, Article 012025, 2021.

[14] A. He, G. Xie, H. Zhang, X. Wang, A comparative study on Johnson–Cook, modified Johnson–Cook and Arrhenius-type constitutive models to predict the high temperature flow stress in 20CrMo alloy steel, Materials & Design (1980–2015), Vol. 52, pp. 677–685, 2013.

[15] Z. Akbari, H. Mirzadeh, J.-M. Cabrera, A simple constitutive model for predicting flow stress of medium carbon microalloyed steel during hot deformation,

Materials & Design, Vol. 77, pp. 126–131, 2015.
[16] A. Ambig, W. Daves, T. Klünsner, B. Thimm, T. Teppernegg, C. Czettl, B. Frunza, T. Antretter, W. Kubin, Modeling High-Speed Milling of Rails for Cost-Efficient Maintenance, Proc 13th Int Conf on Contact Mechanics & Wear of Rail/Wheel Systems , Tokyo, 2025.
[17] B. Thimm, A. Glavas, M. Reuber, H.-J. Christ, Determination of chip speed and shear strain rate in primary shear zone using digital image correlation (DIC) in linear-orthogonal cutting experiments, Journal of Materials Processing Technology, Vol. 289, Article 116957, 2021.